

Phase regulation of Ni-based catalyst promotes selective hydrogenation of furfural: Effect of glycerol and Zn content

Chunyan Yang^a, Changfu Zhuang^{a,*}, Zhouxiao Zhai^a, Xu Zhao^a, Dejin Huang^a, Di Tian^a, Chungang Min^{b,*}, Jie Zhao^c, Ying Wang^{a,*}

^a Key Laboratory of Forest Resources Conservation and Utilization in the Southwest Mountains of China Ministry of Education, Southwest Forestry University, Kunming 650051, PR China

^b Research Center for Analysis and Measurement, Kunming University of Science and Technology, Kunming 650093, PR China

^c Key Laboratory of Bionic Engineering, Ministry of Education, Jilin University, Changchun 130022, PR China



ARTICLE INFO

Keywords:
Ni-based catalyst
Phase regulation
Glycerol
Zn content
furfural
Selective hydrogenation

ABSTRACT

Accurate regulation of active components is of great significance to catalyst design. In this paper, a series of bimetallic carbide catalysts ($\text{Ni}_x\text{Zn}_y@\text{CN-G}$) were prepared using low-cost feed stock by the strategy of glycerol assisting Zn content, in which glycerol and Zn were used as phase modifiers. When used for the selective hydrogenation of biomass furfural (FAL) to furfuryl alcohol (FOL), the FOL yield from the optimum catalyst $\text{Ni}_3\text{Zn}@\text{CN-G}$ was 9 times higher than that of $\text{Ni}@\text{CN}$ without glycerol and Zn incorporation. The superior catalytic performance is ascribed to the high content of single $\text{Ni}_3\text{ZnC}_{0.7}$ phase in the catalyst. The characterization and DFT calculation show that $\text{Ni}_3\text{ZnC}_{0.7}$ phase promotes the activation of H_2 and FAL. More importantly, the composition and content of catalyst phase can be adjusted by the Zn content change and glycerol assistance. Meanwhile, the effects of glycerol and Zn content on the catalytic reaction are discussed in detail. This work reveals the correlation between phase regulation and catalytic performance, which provides a new idea for phase design of catalysts and catalytic conversion of biomass.

1. Introduction

Renewable biomass is an ideal raw material for the production of chemicals. Furfural (FAL) can be used as a link between biomass resources and chemical industry. Furfuryl alcohol (FOL) is an important hydrogenation product of FAL, and about 65 % of FAL is used to produce FOL. It is widely used in the production of synthetic resins, reaction solvents and chemicals [1,2]. At present, many heterogeneous catalysts have been reported to catalyze the hydrogenation of FAL to FOL [3–5]. Among them, Ni-based catalysts have attracted much attention because of their low cost and excellent catalytic hydrogenation activity. However, the electronic structure and geometric structure of Ni can simultaneously activate the $\text{C}=\text{C}$ and $\text{C}=\text{O}$ bonds of FAL, which leads to excessive hydrogenation to tetrahydrofurfuryl alcohol. Moreover, since Ni's activity is lower than that of noble metals, harsh reaction conditions, such as high temperature and a lengthy time period, are necessary. Therefore, creating a Ni-based catalyst with good performance under mild conditions is quite difficult.

The catalytic performance is closely related to the active phase

structure in the catalyst [6]. Because of their catalytic performance comparable to that of noble metals in many significant reactions, transition metal carbides have garnered increased interest [7–12]. The unique conformation of the active phase in metal carbides can modulate their catalytic performance. Owing to Ni's high activity, it is vital to control the structure of metal active components in order to produce hydrogenation products with a high degree of selectivity [13]. Generally, the position of carbon atoms can be adjusted on the gap position or surface of Ni [14,15]. Whenever the chemical potential of the reaction molecules sufficiently high, the free atoms fill the interstitial places of transition metal catalysts [16–18]. This can alter the electronic and geometric characteristics of the surface atoms [19], which will regulate the catalytic activity of olefins [20]. Zhang's research shows that the composition and structure of Ni-based carbides are systematically regulated, which can improve the activity and stability of methane steam reforming reaction [21]. Doping with transition metals is an additional intriguing approach for modifying the catalytic efficacy of metal carbide. The addition of the second metal can form an alloy that, through electrical and geometrical effects, can adjust the active sites of

* Corresponding authors.

E-mail addresses: cfzhuang@swfu.edu.cn (C. Zhuang), minchungang@163.com (C. Min), yingwang@swfu.edu.cn (Y. Wang).

Ni [22–25]. By introducing two metal components into the carbide lattice, such as Ni, Zn, Fe and Co, bimetallic carbides can be formed. Bimetallic carbide catalysts typically exhibit superior catalytic performance than the corresponding monometallic carbides [26]. Smirnov et al. prepared a series of Ni-Mo carbide catalysts. Among various phases such as Ni-Mo bimetallic phase and Mo carbide, the Ni-Mo alloy phase exhibits the maximum activity [27]. The structure of active phase will affect the accessibility of reactants to active sites, which plays a decisive role in catalytic performance [6,28–31]. However, due to the lack of awareness concerning the active site structure and the structure-activity relationship, the design and preparation of high-performance Ni-based catalysts are limited.

Furthermore, the catalyst's active phase composition can be precisely managed to control the adsorption and activation of reactants. Investigating the controlled production of metal-carbon phases is therefore important. However, despite reports that chemical vapor deposition has enabled the controlled synthesis of phase composition in metal carbides [32], arc discharge [33], temperature programmed reduction of gas carbon source [34] and other methods. Unfortunately, there are several drawbacks to the traditional preparation method of single phase composition, including high preparation costs, a difficult procedure, etc. In particular, it must experience high pollution and high energy consumption. This significantly restricts the use of this catalytic material [32]. Consequently, it is challenging to come with an inexpensive and feasible approach to accurately regulate the phase composition of metal carbides.

In this work, Ni-based metal catalysts with high activity and selectivity were obtained by adjusting the phase composition. The $\text{Ni}_3\text{Zn}@\text{CN-G}$ catalyst with single active phase $\text{Ni}_3\text{ZnC}_{0.7}$ was prepared by using glycerol and Zn content as phase regulators. In this paper, the effect of glycerol and Zn content on the regulation of the phase was investigated in detail. The best $\text{Ni}_3\text{Zn}@\text{CN-G}$ was used for selective catalysis of FAL, and FOL yield was 9 times that of $\text{Ni}@\text{CN}$ without glycerol and Zn doping. The structure-activity relationship between the phase composition and catalytic performance of Ni-based catalyst was deeply studied by correlation characterization and DFT theoretical calculation. This work deepens the understanding of bimetallic carbide as the active phase of catalytic reaction.

2. Experiment part

2.1. Materials

$\text{Ni}(\text{NO}_3)_2 \cdot 6\text{H}_2\text{O}$ (99.0 %), $\text{Zn}(\text{NO}_3)_2 \cdot 6\text{H}_2\text{O}$ (99.0 %) and Fumaric Acid (99.0 %) were purchased from Adamas Reagent Co. FAL was purchased from TCI (Shanghai) Development Co. Glycerol, isopropanol (99.7 %) and ethanol (99.7 %) were purchased from Sinopharm Chemical Reagent Co. All the chemicals used in this experiment were ready to use without further treatment.

2.2. Preparation of catalysts

2.2.1. Preparation of $\text{Ni}_x\text{Zn}_y@\text{CN-G}$

Urea (14 mmol), fumaric acid (2.5 mmol), $\text{Ni}(\text{NO}_3)_2 \cdot 6\text{H}_2\text{O}$ (1.5 mmol) and $\text{Zn}(\text{NO}_3)_2 \cdot 6\text{H}_2\text{O}$ were put into 40 mL glycerol and stirred for 12 h, in which the molar amount of added Ni was fixed, while the amount of Zn was added at $\text{Ni}/\text{Zn} = 10:0, 10:1, 3:1, 2:1$ and $1:1$, corresponding to $\text{Ni}@\text{CN-G}$, $\text{Ni}_{10}\text{Zn}@\text{CN-G}$, $\text{Ni}_3\text{Zn}@\text{CN-G}$, $\text{Ni}_2\text{Zn}@\text{CN-G}$, $\text{NiZn}@\text{CN-G}$. 20 mL of the evenly stirred mixture is poured into a magnetic boat and put into a tubular furnace. The temperature was programmed from room temperature to 600°C at the rate of 5°C min^{-1} in Ar atmosphere, kept for 2 h, and finally naturally cooled to room temperature. The obtained samples was abbreviated as $\text{Ni}_x\text{Zn}_y@\text{CN-G}$.

2.2.2. Preparation of $\text{Ni}_x\text{Zn}_y@\text{CN}$

Urea (14 mmol), fumaric acid (2.5 mmol) and deionized water (60

mL) were added to the beaker and stirred for 2 h. Then, $\text{Ni}(\text{NO}_3)_2 \cdot 6\text{H}_2\text{O}$ (1.5 mmol) and $\text{Zn}(\text{NO}_3)_2 \cdot 6\text{H}_2\text{O}$ were added, in which the molar amount of Ni was fixed, while the amount of Zn was in the ratio of $\text{Ni}/\text{Zn} = 10:0, 10:1, 3:1$ and $2:1$. The uniform mixed solution stirred for 1.5 h was poured into the reaction kettle and heated in the oven at 120°C for 6 h. The separated solid powder was washed three times with deionized water and ethanol respectively, and finally dried in vacuum at 80°C for 12 h. The prepared sample was noted as $\text{Ni}_x\text{Zn}_y-\text{MOF}$.

0.5 g $\text{Ni}_x\text{Zn}_y-\text{MOF}$ is placed in a magnetic boat and placed in a tube furnace. In Ar atmosphere, the room temperature was programmed to 600°C at the rate of 5°C min^{-1} , kept heating for 2 h, and finally naturally cooled to room temperature. The calcined sample was recorded as $\text{Ni}_x\text{Zn}_y@\text{CN}$.

2.3. Characterization methods

Transmission electron microscopy (TEM) and electron diffraction detection were performed on a FEI Talos F200X American FEI instrument. The average particle size was calculated statistically on the software Nano Measurer 1.2 by selecting 100–180 particles from the TEM images. High-angle annular dark-field scanning transmission electron microscopy (HAADF-STEM) images were imaged by an FEI Talos-F200S model at 300 kV equipped with an energy dispersive X-ray spectrometer (EDS). X-ray photoelectron spectroscopy (XPS) analysis was performed with a monochromatic $\text{Al K}\alpha$ X-ray source at 50 W, 15 KV on a PHI5000 Versaprobe II scanning XPS microprobe system. XPS spectra were fitted on the software MultiPak to analyze all elemental compositions and chemical species in the samples, with binding energy based on a C 1s peak at 284.8 eV. Powder X-ray diffraction (XRD) spectra were recorded at 40 kV and 40 mA on a Rigaku Ultima X-ray diffraction spectrometer using copper $\text{K}\alpha$ radiation ($\lambda = 1.5418 \text{ \AA}$). The specific surface area and pore characteristics of the catalysts were characterized by N_2 adsorption-desorption measurements at 77 K using an ASAP 2020 Plus physisorption instrument with Brunauer-Emmet-Teller (BET) test method. The metal content of the samples was measured by inductively coupled plasma emission spectrometry (ICP-OES) using a VISTA-MPX instrument.

Programmed temperature rise reduction (TPR) of H_2 and programmed temperature rise desorption (TPD) of NH_3 and H_2 were performed in a tp-5080 China Xianquan chemisorber equipped with a thermal conductivity detector (TCD). In the H_2 -TPR routine test, the carrier gas was first pre-treated in an Ar gas stream (30 mL min^{-1}) at a rate of $10^\circ\text{C min}^{-1}$ to 200°C for 1 h, and then lowered to room temperature. After the temperature stabilization, the carrier gas was switched to an H_2/Ar mixture (30 mL min^{-1}) and purged for 1 h. After the baseline stabilization, the temperature was ramped up to 800°C at a rate of $10^\circ\text{C min}^{-1}$, and the signal was recorded every 1 s. The signal was recorded ten times. In the TPD test, the carrier/reference gas was first pre-treated in helium (30 mL min^{-1}) at a rate of $10^\circ\text{C min}^{-1}$ to 150°C for 1 h, then lowered to the adsorption temperature of 100°C , and after the temperature stabilization, the carrier/reference gas was switched to the adsorption gas and adsorbed at a flow rate of 30 mL min^{-1} for 1 h. Then, the carrier gas was switched to helium (30 mL min^{-1}) and purged for 1 h. After the baseline was stabilized, the temperature was increased to 700°C at a rate of $10^\circ\text{C min}^{-1}$, and the signal was recorded ten times every 1 s. The Raman spectra of the samples are tested by a WiTech alpha 300 R Raman spectrometer with the excitation wavelength of 532 nm. The single spectrum testing conditions are as follows: Laser energy 2.0 mW, 300 g/mm grating, Olympus 20x objective lens (Olympus 20x / 0.25), integration time 20–30 s, 10 times of accumulation.

The Vienna Ab-initio Simulation Package (VASP) program is used for all density generalized function theory calculations. The generalized gradient approximation of the Perdew-Burke-Ernzerhof (PBE) generalized function is applied to all descriptions of the exchange correlations. The cutoff energy of the plane wave basis group is 400 eV and the force

threshold used for all atoms is below $-0.03 \text{ eV}\cdot\text{\AA}^{-1}$. A $3 \times 3 \times 1$ k-point grid of the Brillouin zone is used. To reduce the interaction between periodic thin layers, a vacuum layer of 15 \AA was set up along the Z-direction. The adsorption energies (E_{ads}) of furfural and hydrogen were defined by the following equations: Where E_{total} is the total energy of the ideal surface containing the adsorbate; E_{slab} is the energy of the ideal surface, and E_g is the energy of FAL and H_2 in the gas phase, respectively. At last, Bader charge is computed based on the Bader theory in order to analyze charges transfer [35].

2.4. Catalyst performance evaluation

The catalytic reaction took place in a 25 mL autoclave reactor equipped with a magnetic stirrer and a temperature controller, to which catalyst (25 mg), FAL (96 mg) and isopropanol (8 mL) were added. The reactor was first purged three times repeatedly with H_2 and then pressurized to 2 MPa . The parameters of the reaction (reaction time and temperature) were set in the autoclave, and then the temperature was increased at a certain rate and maintained for a certain time (h) with a stirring speed of 800 rpm .

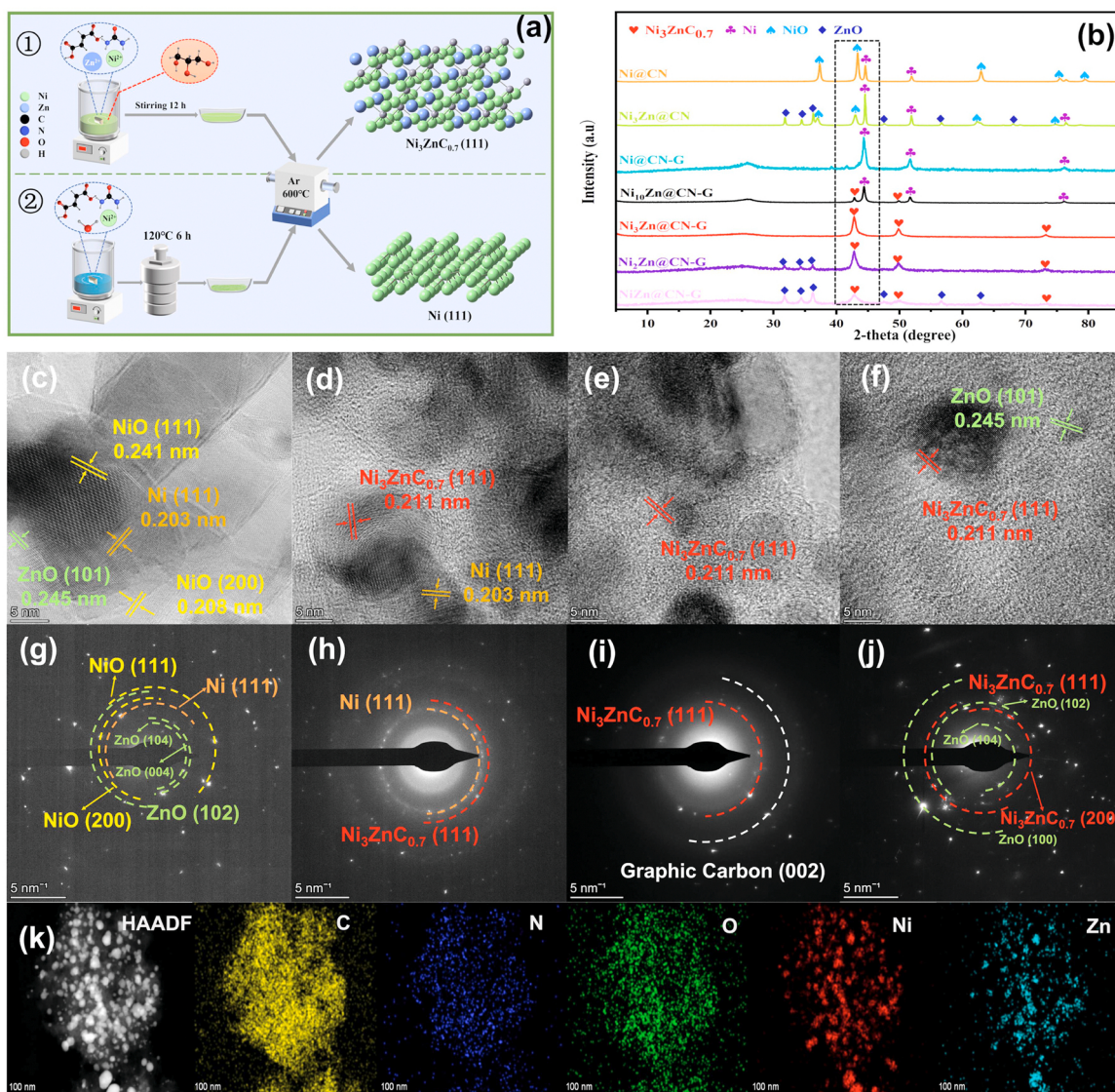


Fig. 1. (a) Synthesis roadmap of $\text{Ni}_x\text{Zn}_y@\text{CN}$ and $\text{Ni}_x\text{Zn}_y@\text{CN-G}$; (b) powder XRD spectra of $\text{Ni}@\text{CN}$, $\text{Ni}_3\text{Zn}@\text{CN}$ and $\text{Ni}_x\text{Zn}_y@\text{CN-G}$ samples; (c–f) HR-TEM diagram: (c) $\text{Ni}_3\text{Zn}@\text{CN}$, (d) $\text{Ni}_{10}\text{Zn}@\text{CN-G}$, (e) $\text{Ni}_3\text{Zn}@\text{CN-G}$, (f) $\text{NiZn}@\text{CN-G}$; (g–j) SAED diagram: (g) $\text{Ni}_3\text{Zn}@\text{CN}$, (h) $\text{Ni}_{10}\text{Zn}@\text{CN-G}$, (i) $\text{Ni}_3\text{Zn}@\text{CN-G}$, (j) $\text{NiZn}@\text{CN-G}$; (k) EDS elemental mapping of $\text{Ni}_3\text{Zn}@\text{CN-G}$.

After the reaction was cooled to room temperature, the reacted catalyst was collected by filtration, washed three times with ethanol, and then dried under vacuum at 80°C for 6 h for use in subsequent cyclic experiments. The products were distinguished by GC-MS and quantified by GC (GC-7890A, Agilent). The conversion of reactants and selectivity of target products were calculated by internal standard method. Where the conversion (%) and selectivity (%) calculated by the following equation, respectively:

$$\text{Conversion (\%)} = \frac{\text{Mole of FAL converted}}{\text{Mole of FAL loaded}} \times 100\% \quad (2)$$

$$\text{Selectivity (\%)} = \frac{\text{Mole of FOL produced}}{\text{Mole of product produced}} \times 100\% \quad (3)$$

3. Results and discussion

3.1. Synthesis and characterization of materials

3.1.1. Effect of glycerol and Zn doping on phase composition

Fig. 1a shows two synthetic routes of Ni-based catalyst with and

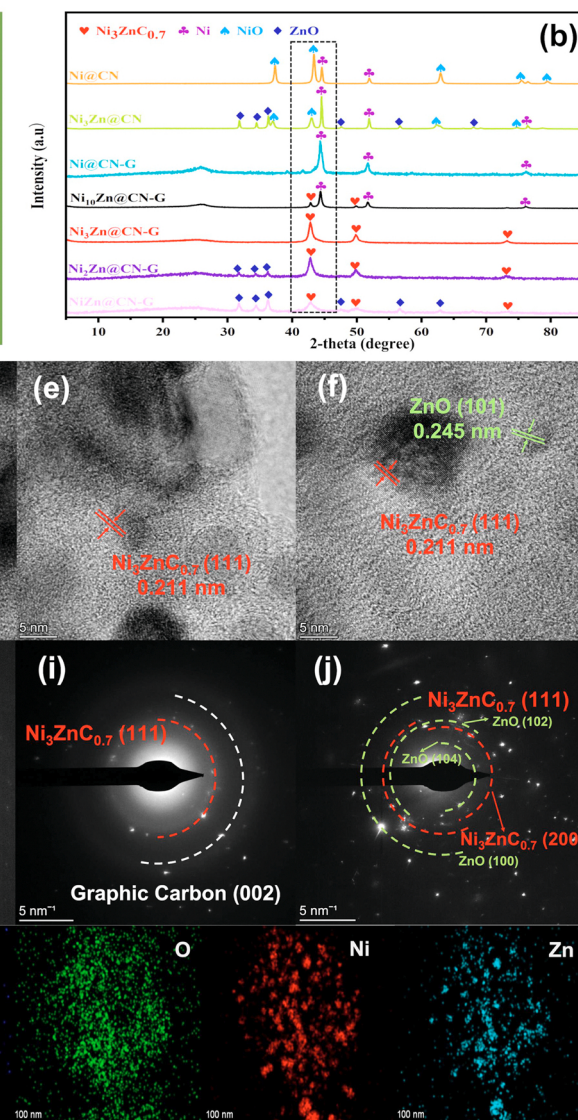


Fig. 1. (a) Synthesis roadmap of $\text{Ni}_x\text{Zn}_y@\text{CN}$ and $\text{Ni}_x\text{Zn}_y@\text{CN-G}$; (b) powder XRD spectra of $\text{Ni}@\text{CN}$, $\text{Ni}_3\text{Zn}@\text{CN}$ and $\text{Ni}_x\text{Zn}_y@\text{CN-G}$ samples; (c–f) HR-TEM diagram: (c) $\text{Ni}_3\text{Zn}@\text{CN}$, (d) $\text{Ni}_{10}\text{Zn}@\text{CN-G}$, (e) $\text{Ni}_3\text{Zn}@\text{CN-G}$, (f) $\text{NiZn}@\text{CN-G}$; (g–j) SAED diagram: (g) $\text{Ni}_3\text{Zn}@\text{CN}$, (h) $\text{Ni}_{10}\text{Zn}@\text{CN-G}$, (i) $\text{Ni}_3\text{Zn}@\text{CN-G}$, (j) $\text{NiZn}@\text{CN-G}$; (k) EDS elemental mapping of $\text{Ni}_3\text{Zn}@\text{CN-G}$.

without glycerol. In the preparation process of route 1, a series of bimetallic NiZn carbide catalysts ($\text{Ni}_x\text{Zn}_y@\text{CN-G}$) were prepared by a new strategy of glycerol-assisted Zn content regulation. The glycerol mixture of metal salt and organic ligand stirred at room temperature for a certain time was directly put into a tubular furnace for calcination. However, route 2 is that the solid materials synthesized by hydrothermal method are put into a tubular furnace for calcination. Compared with route 2, route 1 is not only operated at room temperature, but also has simple steps. More importantly, the phase composition can be regulated by introducing glycerol and adjusting Zn content.

To understand the regulation of Zn content on phase composition, XRD of $\text{Ni}_x\text{Zn}_y@\text{CN-G}$ sample is shown in Fig. 1b. The three characteristic diffraction peaks in the XRD of $\text{Ni}@\text{CN-G}$ correspond to the (111), (200) and (220) crystal planes of Ni (JCPDS No.65–0380), which indicates that there are no carbon atoms in the Ni lattice [36]. After adding various Zn contents, three new diffraction peaks of $\text{Ni}_{10}\text{Zn}@\text{CN-G}$, $\text{Ni}_3\text{Zn}@\text{CN-G}$, $\text{Ni}_2\text{Zn}@\text{CN-G}$ and $\text{NiZn}@\text{CN-G}$ samples occur at 42.7° , 49.7° and 73.0° respectively, which belongs to cubic phase (fcc) $\text{Ni}_3\text{ZnC}_{0.7}$ (JCPDS No. 28–0713). The diffraction peak of $\text{Ni}_x\text{Zn}_y@\text{CN-G}$ shifted to a lower 42.7° from 44.3° of Ni (111) in $\text{Ni}@\text{CN-G}$. This demonstrates that Zn atoms enter the metallic Ni lattice [37]. In $\text{Ni}_{10}\text{Zn}@\text{CN-G}$, it is mostly made up of $\text{Ni}_3\text{ZnC}_{0.7}$ and metallic Ni. $\text{Ni}_3\text{Zn}@\text{CN-G}$ is composed of one $\text{Ni}_3\text{ZnC}_{0.7}$ phase when the Zn content is increased to a 3:1 Ni to Zn ratio. As the Zn content rises to $\text{Ni}_2\text{Zn}@\text{CN-G}$ and $\text{NiZn}@\text{CN-G}$, new diffraction peaks appear in the spectrum, corresponding to ZnO (JCPDS No.36–1451). Moreover, the higher the Zn content, the stronger ZnO diffraction intensity. As can be shown, altering the Zn content can change the phase composition of the $\text{Ni}_x\text{Zn}_y@\text{CN-G}$ sample.

The effect of glycerol addition on the formation of $\text{Ni}_3\text{ZnC}_{0.7}$ phase is explored. Comparing synthesis routes 1 and 2 of Ni-based catalysts, the most significant difference is the participation of glycerol (Fig. 1a). In XRD of $\text{Ni}_3\text{Zn}@\text{CN}$ without glycerol, in addition to the three typical Ni diffraction peaks (JCPDS No.65–0380), there are also NiO (JCPDS No.47–1049) and ZnO (JCPDS No.36–1451) diffraction peaks. However, only the $\text{Ni}_3\text{ZnC}_{0.7}$ phase can be seen in the XRD pattern of $\text{Ni}_3\text{Zn}@\text{CN-G}$ produced with glycerol. The explanation could be that enough glycerol filled the ligand left over after pyrolysis, causing carbon to diffuse and stabilize in the gap position of the Ni-based structure and creating the distinctive gap structure of $\text{Ni}_3\text{ZnC}_{0.7}$ [19]. Therefore, glycerol must be added in order for the $\text{Ni}_3\text{ZnC}_{0.7}$ phase to develop.

HR-TEM and electron diffraction patterns clearly show the phase structure of the samples. Firstly, the effect of glycerol on the crystal lattice of the sample was discussed. In $\text{Ni}_3\text{Zn}@\text{CN}$ without glycerol (Fig. 1c) exhibits the (111), (220) crystalline planes of NiO and the (111) crystalline planes of Ni. While in Fig. 1d–f, the HR-TEM image of $\text{Ni}_{10}\text{Zn}@\text{CN-G}$, $\text{Ni}_3\text{Zn}@\text{CN-G}$ and $\text{NiZn}@\text{CN-G}$ with glycerol can identify the lattice spacing of 0.211 nm corresponding to the $\text{Ni}_3\text{ZnC}_{0.7}$ (111) crystal plane [38], which further proves that glycerol is required for the formation of $\text{Ni}_3\text{ZnC}_{0.7}$ phase. Meanwhile, the addition of carbon atoms was confirmed by the increase of the interplanar spacing from Ni (111) to $\text{Ni}_3\text{ZnC}_{0.7}$ (111). Subsequently, the phase composition of $\text{Ni}_x\text{Zn}_y@\text{CN-G}$ with different Zn contents were presented. The crystallographic changes in the HR-TEM images of $\text{Ni}@\text{CN-G}$ to $\text{NiZn}@\text{CN-G}$ (Fig. 1d–f) also provide sufficient evidence that the Zn content can modulate the phase composition of $\text{Ni}_x\text{Zn}_y@\text{CN-G}$ samples. This is completely consistent with XRD analysis of phase composition. Among them, the selected area electron diffraction (SAED) maps (Fig. 1g–j) show the diffraction rings corresponding to each lattice face of each catalyst sample, which are in good agreement with the XRD results. In addition, supporting the formation of the $\text{Ni}_3\text{ZnC}_{0.7}$ phase is the EDS element mapping (Fig. 1g), which demonstrates the uniform distribution of the C, Ni, and Zn elements of $\text{Ni}_3\text{Zn}@\text{CN-G}$, and the elements are highly coincident.

The effects of glycerol and different Zn contents were analyzed by XPS. First, the effect of zinc incorporation was discussed. In the Ni 2p

spectrum, the peak of Ni^{2+} is attributed to the surface oxidation caused by air exposure [39]. suggesting that the introduction of Zn leads to an increase in Ni electron density in $\text{Ni}_x\text{Zn}_y@\text{CN}$ [32]. Compared with Ni^0 species (852.72 eV) in $\text{Ni}@\text{CN}$, the binding energy of Ni 2p_{3/2} in Zn-doped $\text{Ni}_x\text{Zn}_y@\text{CN}$ gradually decreases, which indicated that the introduction of Zn led to the increase of the Ni electron density in $\text{Ni}_x\text{Zn}_y@\text{CN-G}$ [32]. In addition, the phase transition from $\text{Ni}@\text{CN-G}$ to $\text{Ni}_{10}\text{Zn}@\text{CN-G}$ also shows that Zn addition is an important factor for the formation of $\text{Ni}_3\text{ZnC}_{0.7}$ phase [38]. Simultaneously, different Zn content has obvious influence on the content of $\text{Ni}_3\text{ZnC}_{0.7}$ phase in $\text{Ni}_x\text{Zn}_y@\text{CN-G}$. Because the Ni content in $\text{Ni}_x\text{Zn}_y@\text{CN-G}$ is the same, the content of $\text{Ni}_3\text{ZnC}_{0.7}$ phase on their surfaces was analyzed by XPS. The variation trend of $\text{Ni}_3\text{ZnC}_{0.7}$ content in $\text{Ni}_x\text{Zn}_y@\text{CN-G}$ is as follows: $\text{Ni}_3\text{Zn}@\text{CN-G}$ (53.56 %) > $\text{Ni}_2\text{Zn}@\text{CN-G}$ (41.84 %) > $\text{NiZn}@\text{CN-G}$ (34.27 %) > $\text{Ni}_{10}\text{Zn}@\text{CN-G}$ (10.74 %).

Next, the effect of glycerol was explored by comparing the XPS spectra of Ni 2p and Zn 2p. Both Ni 2p_{3/2} (Fig. 2a) and Zn 2p_{3/2} (Fig. 2b) binding energies of $\text{Ni}_x\text{Zn}_y@\text{CN-G}$ are higher than those of $\text{Ni}_x\text{Zn}_y@\text{CN}$, indicating that the addition of glycerol causes Ni and Zn to lose electrons. This is consistent with the Bader charge analysis (Table 1). Both Ni and Zn are electron deficient in $\text{Ni}_3\text{ZnC}_{0.7}$ (-0.24 and -0.49 e), indicating electron transfer from metal to carbon, which is consistent with literature reports [39]. In the C 1s spectrum (Fig. 2c), the addition of glycerol causes the binding energy of carbon to shift to a higher position, which may be due to a change in the carbon environment due to the difference between the two different preparation routes [40,41]. The structure and properties of the carbon species on the samples were further investigated by Raman spectroscopy. As seen in Fig. 2d, $\text{Ni}_x\text{Zn}_y@\text{CN-G}$ appears as distinct D and G bands located at 1340 cm^{-1} and 1590 cm^{-1} compared to both $\text{Ni}@\text{CN}$ and $\text{Ni}_3\text{Zn}@\text{CN}$ [42,43]. This indicates a strong interaction between carbon and metal during the preparation process, resulting in a significant change in the carbon surroundings [44,45]. It can be seen that the addition of glycerol led to a increase in graphitization and defects in $\text{Ni}_x\text{Zn}_y@\text{CN-G}$, which improved the mobility of electrons and the adsorption of substrates [46–49]. Combined with XRD, XPS and Raman spectra, the C atoms in glycerol influence the surrounding electron environment and gradually accumulate to participate in the formation of $\text{Ni}_3\text{ZnC}_{0.7}$ phase [39,50].

3.1.2. Effect of glycerol and Zn doping on structural characteristics

On the average size of metal NPs, the effects of glycerol and Zn doping are discussed. Firstly, Table 2 and Fig. 3 display the average particle size of $\text{Ni}_x\text{Zn}_y@\text{CN-G}$ samples with varied Zn content. The mean particle size of $\text{Ni}_x\text{Zn}_y@\text{CN-G}$ is: $\text{Ni}@\text{CN-G}$ (24 nm) > $\text{Ni}_3\text{Zn}@\text{CN-G}$ (18.47 nm) > $\text{Ni}_2\text{Zn}@\text{CN-G}$ (13.03 nm) > $\text{NiZn}@\text{CN-G}$ (7.49 nm). It is evident that the average metal NPs particle size in $\text{Ni}_x\text{Zn}_y@\text{CN-G}$ reduces as Zn content rises. The reason could be that some metal Zn is volatilized during the high-temperature pyrolysis, which causes the sample particles disperse more evenly, and the formed ZnO also hinders the agglomeration of metal NPs [51–53]. Secondly, glycerol also has an important influence on the particle size of the Ni-based catalysts. According to TEM images, average particle size: $\text{Ni}_3\text{Zn}@\text{CN-G}$ < $\text{Ni}_3\text{Zn}@\text{CN}$ (18.47 nm Vs 28.01 nm), $\text{Ni}@\text{CN}$ and $\text{Ni}@\text{CN-G}$ also showed the same trend (41.96 nm Vs 24.00 nm). This can be seen, the $\text{Ni}_x\text{Zn}_y@\text{CN-G}$ sample with glycerol demonstrated homogeneous metal NPs dispersion in contrast to the evident metal agglomeration of $\text{Ni}_x\text{Zn}_y@\text{CN}$. The main reason for the metal agglomeration caused by the absence of glycerol is the departure of a large number of organic ligands during high-temperature calcination, which weakens the spacing between the remaining ligands and metal NPs [54]. Thus, the involvement of glycerol and different Zn contents can modulate the average particle size of metal NPs.

The effects of glycerol and Zn doping on specific surface area and pore volume are discussed. First, the adsorption isotherms of $\text{Ni}_x\text{Zn}_y@\text{CN-G}$ and $\text{Ni}_x\text{Zn}_y@\text{CN}$ samples with different Zn contents were investigated in Fig. 3g. The adsorption-desorption curves of nitrogen are

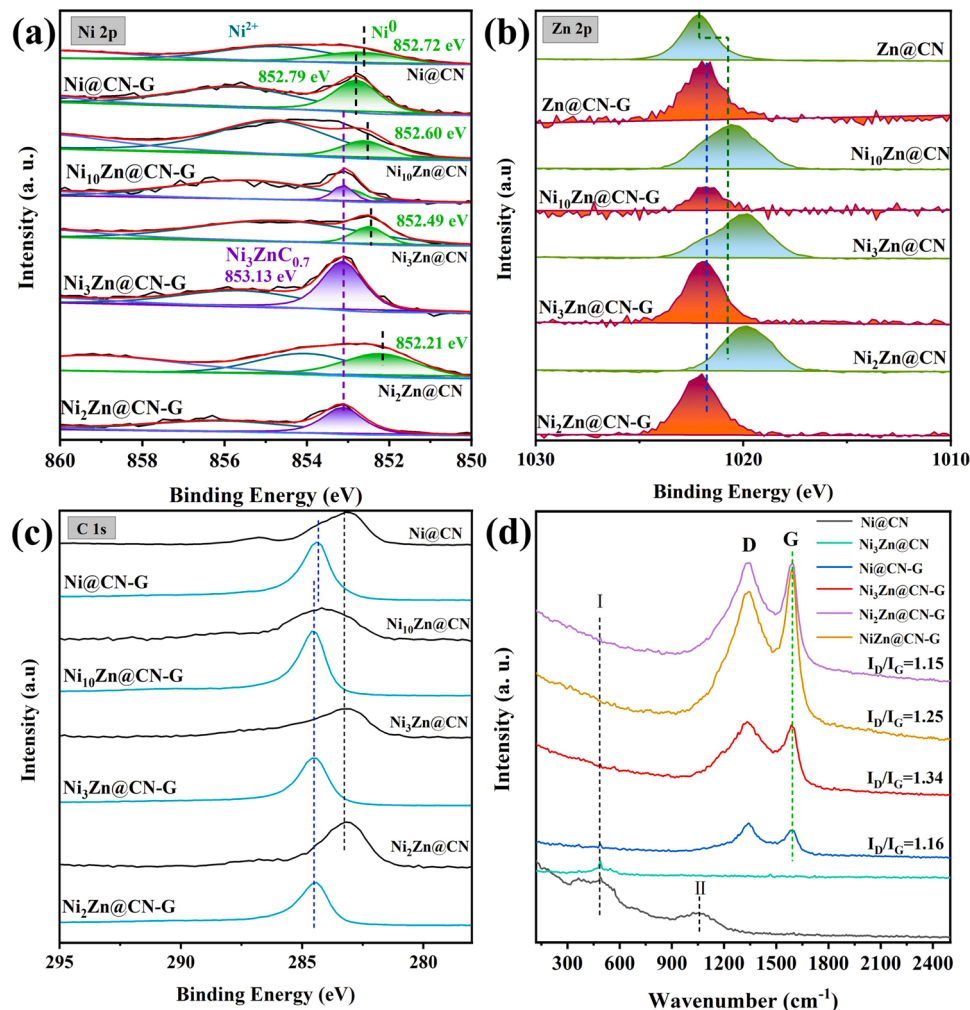


Fig. 2. (a) XPS pattern of Ni 2p of $\text{Ni}_x\text{Zn}_y@\text{CN}$ and $\text{Ni}_x\text{Zn}_y@\text{CN-G}$; (b) XPS pattern of Zn 2p of $\text{Ni}_x\text{Zn}_y@\text{CN}$ and $\text{Ni}_x\text{Zn}_y@\text{CN-G}$; (c) XPS pattern of C 1s of $\text{Ni}_x\text{Zn}_y@\text{CN}$ and $\text{Ni}_x\text{Zn}_y@\text{CN-G}$; (d) The Raman spectrum of $\text{Ni}_x\text{Zn}_y@\text{CN}$ and $\text{Ni}_x\text{Zn}_y@\text{CN-G}$.

Table 1
Bader charge analysis of Ni and $\text{Ni}_3\text{ZnC}_{0.7}$.

	Ni	Zn	C
Ni	-0.04 e		
$\text{Ni}_3\text{ZnC}_{0.7}$	-0.24 e	-0.39 e	0.60 e

all types IV, accompanied by obvious hysteresis loops. This indicates that all samples contain micro-mesoporous structures. As shown in the chart (Fig. 3g-h and Table 2), the specific surface area of $\text{Ni}_x\text{Zn}_y@\text{CN-G}$ increases with the increase of Zn content, compared with $116 \text{ m}^2 \text{ g}^{-1}$ of $\text{Ni}@{\text{CN}}\text{-G}$ without Zn. This implies that the volatilization of Zn during

high temperature pyrolysis is beneficial to an increase in its specific surface area [55,56]. Next, the introduction of glycerol greatly increased the specific surface area from $\text{Ni}_2\text{Zn}@{\text{CN}}$ ($21 \text{ m}^2 \text{ g}^{-1}$) to $\text{Ni}_3\text{Zn}@{\text{CN-G}}$ ($172 \text{ m}^2 \text{ g}^{-1}$). Similarly, the $13 \text{ m}^2 \text{ g}^{-1}$ at $\text{Ni}@{\text{CN}}$ increased to $116 \text{ m}^2 \text{ g}^{-1}$ at $\text{Ni}@{\text{CN-G}}$. The same trend is reflected in the porosity of the material (Table 2). As a result, the introduction of glycerol and Zn with various contents substantially increases the specific surface area and pore volume of $\text{Ni}_3\text{Zn}@{\text{CN-G}}$.

3.2. Catalytic performance of the material

3.2.1. Effect of phase composition regulation on catalytic performance

Reaction conditions: FAL, 96 mg; catalyst, 25 mg; 2-propanol, 8 mL;

Table 2
Structural parameters of $\text{Ni}_x\text{Zn}_y@\text{CN-G}$ catalyst samples and Ni surface chemical composition.

Samples	S_{BET} ($\text{m}^2 \text{ g}^{-1}$)	Pore Volume ^a ($\text{cm}^3 \text{ g}^{-1}$)	Pore Size ^a (nm)	Metal particle size (nm) ^b	$\text{Ni}_3\text{ZnC}_{0.7}^c$	Ni^{0c}	NiO^c	Ni (wt %) ^d	Zn (wt %) ^d
$\text{Ni}@{\text{CN}}$	13	0.07	17.2	41.96	–	14.58	–	76.64	–
$\text{Ni}_3\text{Zn}@{\text{CN}}$	21	0.14	22.5	28.01	–	22.65	77.35	54.89	19.45
$\text{Ni}@{\text{CN-G}}$	116	0.36	15.0	24.00	–	26.84	73.16	45.03	–
$\text{Ni}_{10}\text{Zn}@{\text{CN-G}}$	135	0.30	10.4	21.93	10.74	10.52	78.74	–	–
$\text{Ni}_3\text{Zn}@{\text{CN-G}}$	172	0.31	8.0	18.47	53.56	–	46.44	23.30	4.76
$\text{Ni}_2\text{Zn}@{\text{CN-G}}$	253	0.33	5.3	13.03	41.84	–	58.16	21.32	5.40
$\text{NiZn}@{\text{CN-G}}$	302	0.62	8.7	7.49	34.27	–	65.73	9.51	7.07

a: by ASAP 2020 Plus. b: by TEM. c: by XPS analysis. d: by ICP-OES.

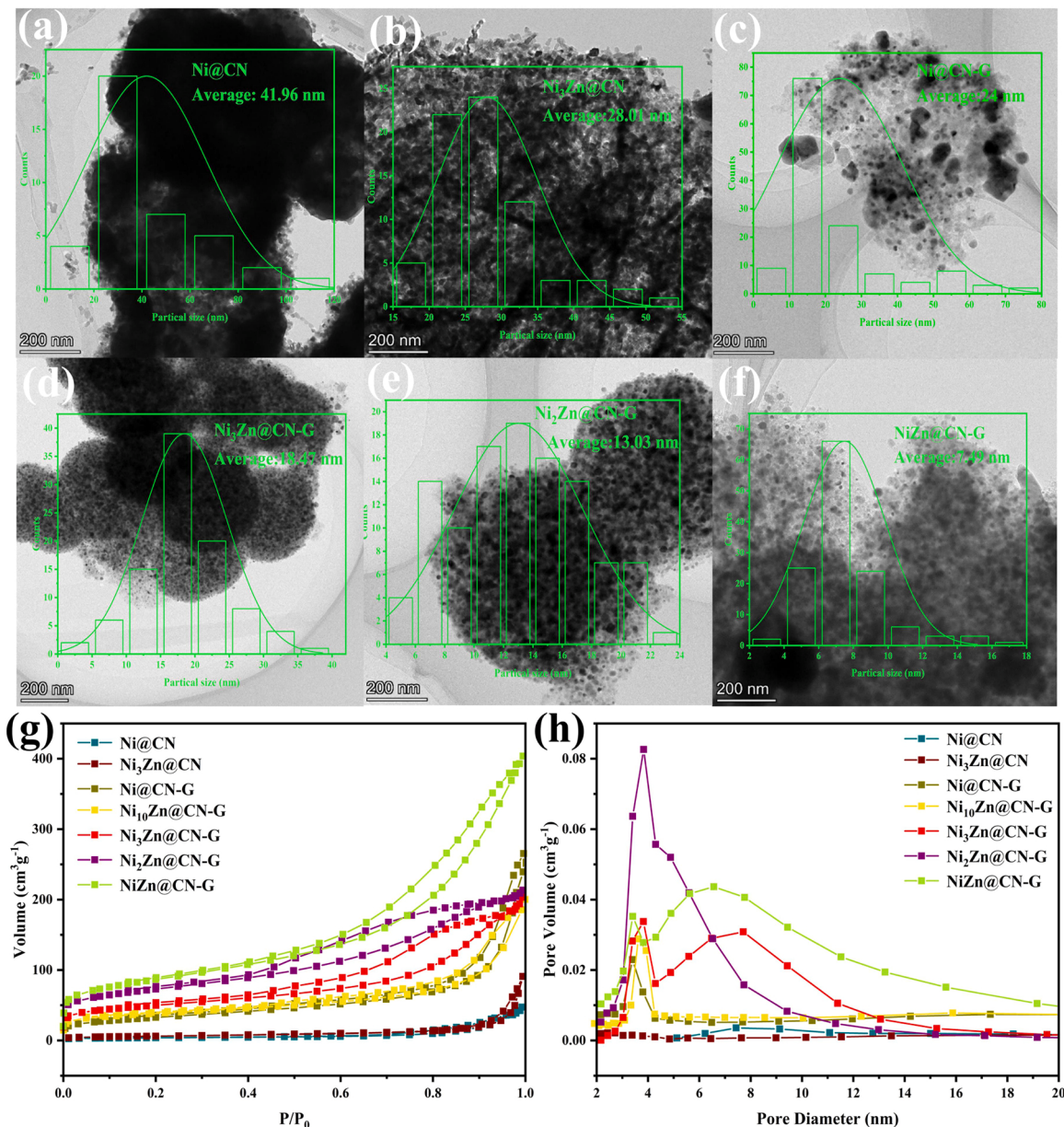


Fig. 3. TEM and particle size of $\text{Ni}_x\text{Zn}_y@\text{CN-G}$ catalyst sample: (a) $\text{Ni}@\text{CN}$, (b) $\text{Ni}_3\text{Zn}@\text{CN}$, (c) $\text{Ni}@\text{CN-G}$, (d) $\text{Ni}_3\text{Zn}@\text{CN-G}$, (e) $\text{Ni}_2\text{Zn}@\text{CN-G}$, (f) $\text{NiZn}@\text{CN-G}$; (g) Nitrogen adsorption-desorption curves and pore size distribution of $\text{Ni}_x\text{Zn}_y@\text{CN-G}$ catalyst samples (h).

H_2 , 2 MPa; 120 °C; 3 h.

Firstly, the impact of glycerol addition on catalytic performance is discussed. The average particle size and specific surface area of the catalyst has important influence on the catalytic performance. Compared with 48.01 nm and $13 \text{ m}^2 \text{ g}^{-1}$ of $\text{Ni}@\text{CN}$, the particle size and specific surface area of $\text{Ni}@\text{CN-G}$ are changed to 24 nm and $116 \text{ m}^2 \text{ g}^{-1}$, respectively, which is highly helpful to enhance the catalytic performance. In addition, the Ni^0 content of $\text{Ni}@\text{CN-G}$ (26.84 %) is higher than that of $\text{Ni}@\text{CN}$ (14.58 %) (Table 2). The catalytic yields of $\text{Ni}@\text{CN}$ and $\text{Ni}@\text{CN-G}$, however, are 10.0 % and 15.2 %, respectively (Table 3, entry 2 and 5). The reason may be that the active site of $\text{Ni}@\text{CN-G}$ is Ni^0 phase, while $\text{Ni}@\text{CN}$ is Ni^0 and NiO phase. Similarly, distinct phases could be the source of the difference in catalytic efficacy between $\text{Ni}_3\text{Zn}@\text{CN}$ and $\text{Ni}_3\text{Zn}@\text{CN-G}$. The catalytic yield of $\text{Ni}_3\text{Zn}@\text{CN-G}$ (91.2 %) is three times that of $\text{Ni}_3\text{Zn}@\text{CN}$ (30.3 %). The addition of glycerol resulted in a smaller particle size (18.47 nm) and a larger specific surface area ($172 \text{ m}^2 \text{ g}^{-1}$) for $\text{Ni}_3\text{Zn}@\text{CN-G}$ compared with 28.01 nm and $21 \text{ m}^2 \text{ g}^{-1}$ of $\text{Ni}_3\text{Zn}@\text{CN}$. However, the phase analysis shows that the mixture

Table 3
Preparation of FOL by FAL catalyzed by different catalysts.

Entry	Sample	Con (%)	Sel (%)	Yield (%)
1	Blank	0	0	0
2	$\text{Ni}@\text{CN}$	13.4	74.6	10.0
3	$\text{Ni}_3\text{Zn}@\text{CN}$	48.5	62.4	30.3
4	$\text{Ni}_2\text{Zn}@\text{CN}$	36.1	89.0	32.1
5	$\text{Ni}@\text{CN-G}$	17.9	85.1	15.2
6	$\text{Ni}_{10}\text{Zn}@\text{CN-G}$	24.3	95.7	23.2
7	$\text{Ni}_3\text{Zn}@\text{CN-G}$	95.0	96.0	91.2
8	$\text{Ni}_2\text{Zn}@\text{CN-G}$	75.3	96.4	72.6
9	$\text{NiZn}@\text{CN-G}$	43.5	97.7	42.5
10	$\text{Zn}@\text{CN-G}$	0	0	0

phase of Ni , NiO and ZnO appear in $\text{Ni}_3\text{Zn}@\text{CN}$, while $\text{Ni}_3\text{Zn}@\text{CN-G}$ only exhibits the single $\text{Ni}_3\text{ZnC}_{0.7}$ phase. Therefore, we speculate that the addition of glycerol leads to the formation of $\text{Ni}_3\text{ZnC}_{0.7}$ phase, which may be the primary factor for the higher catalytic performance of

Ni₃Zn@CN-G.

Then, the effect of different Zn content on the catalytic performance of Ni_xZny@CN-G also lends credence to this argument. It can be seen from Fig. 3a that the specific surface area and average particle size of Ni_xZny@CN catalyst have low correlation with catalytic yield. Ni₂Zn@CN-G and NiZn@CN-G have smaller particle size (13.03 and 7.49 nm) and larger specific surface area (253 and 302 m² g⁻¹). The catalyzed FOL yields were 72.6 % and 42.5 %, respectively. Ni₃Zn@CN-G with medium surface area (172 m² g⁻¹) and particle size (18.47 nm) showed the greatest catalytic performance with FOL yield of 91.2 %. Thus, in light of the correlation between specific surface area and particle size of the catalyst and its catalytic performance, they are not the central factors determining catalytic activity. However, Fig. 3a shows that the catalytic yield is strongly dependent on the Ni/Zn ratio in Ni_xZny@CN-G. The previous structural characterization has proved that different Ni/Zn ratio can control the phase composition of Ni_xZny@CN-G catalyst. This further proves that the phase composition influenced by Ni/Zn ratio is the most critical factor leading to the difference in catalytic performance.

In order to intuitively analyze the effect of phase composition in Ni_xZny@CN-G on catalytic performance, the relationship between the Ni₃ZnC_{0.7} phase content and catalytic performance is explored. As shown in Fig. 4b, the Ni₃ZnC_{0.7} phase content in Ni_xZny@CN-G increases along with the FAL conversion and yield. The yield of Ni₁₀Zn@CN-G with little Zn is only 23.2 %, this is due to the fact that the active component is only 10.74 %. Due to the insufficient amount of Zn, the Ni in Ni₁₀Zn@CN-G is not completely converted into the more active Ni₃ZnC_{0.7} phase. Nevertheless, when the Zn content increased to Ni₂Zn@CN-G and NiZn@CN-G, the yields reached 75.3 % and 43.5 %, as active phase Ni₃ZnC_{0.7} content was 41.84 % and 34.27 %, respectively. The reason is that ZnO generated by excessive Zn covers the active phase Ni₃ZnC_{0.7}, which hinders the adsorption and activation of the reaction substrate. Meanwhile, the higher the Zn content, the more the active phase is covered, which leads to the decrease of activity. As the only Ni₃ZnC_{0.7} phase content reaches the most 53.56 % when the Ni/Zn ratio is raised to an appropriate Ni₃Zn@CN-G, the FOL yield reaches the highest 91.2 %. In conclusion, there is a positive correlation between the Ni₃ZnC_{0.7} phase content and catalytic yield. Hence, the content of Ni₃ZnC_{0.7} phase should be the most important factor affecting the catalytic performance.

3.2.2. Effect of phase composition regulation on hydrogen activation

Activation of H₂ is very important for hydrogenation reaction. The activation ability of catalysts for H₂ is investigated by H₂-TPD. The effect of variation in the amount of Zn was first discussed. The total hydrogen consumption in Ni_xZny@CN-G was ranked in order of magnitude: Ni₃Zn@CN-G (0.219 mmol g⁻¹) > Ni₂Zn@CN-G (0.142 mmol g⁻¹) > NiZn@CN-G (0.115 mmol g⁻¹) > Ni@CN-G (0.040 mmol g⁻¹). This is

consistent with the positive correlation between the Ni₃ZnC_{0.7} phase content and catalytic yield (Fig. 4b). Similar trends were observed for Ni@CN (0.008 mmol g⁻¹) and Ni₃Zn@CN (0.004 mmol g⁻¹). Secondly, the influences of glycerol on the adsorption capacity of H₂ on the catalyst is also studied in Fig. 5a. Compared with Ni@CN and Ni₃Zn@CN, the total amount of H₂ desorbed by Ni@CN-G and Ni₃Zn@CN-G was increased by a factor of 5 and about 55, respectively. This reveals that the addition of glycerol greatly enhances the activation of H₂. This may be due to the addition of glycerol to provide extra carbon source, which helps form the Ni₃ZnC_{0.7} phase in Ni₃Zn@CN-G with higher activity. As a result, the Ni₃ZnC_{0.7} phase content is modulated by the glycerol-assisted Zn content, which can considerably improve the activation of H₂.

As shown in Fig. 5 b, the properties of the catalyst can be further understood by H₂-TPR. Firstly, the effects of Zn addition on Ni@CN-G and Ni₃Zn@CN-G catalysts were investigated. The two reduction peaks of Ni₃Zn@CN-G catalyst moved to 229 °C and 589 °C, respectively, from the Ni@CN-G reduction peaks at 304 °C and 650 °C. This demonstrates how the addition of Zn can lower the reduction temperature of the catalyst. This suggests that the addition of Zn speeds up the reduction of Ni₃ZnC_{0.7} phase, which may be the result of hydrogen overflow [57]. Compared with 0.445 mmol g⁻¹ of Ni@CN-G, the total hydrogen consumption of Ni₃Zn@CN-G is 1.356 mmol g⁻¹, which is 3 times that of Ni@CN-G. Then, the effects of glycerol addition on Ni₃Zn@CN and Ni₃Zn@CN-G catalysts are discussed. The hydrogen consumption of Ni₃Zn@CN-G is increased to 1.356 mmol g⁻¹ from 0.201 mmol g⁻¹ of Ni₃Zn@CN. The addition of glycerol leads to the hydrogen consumption of Ni₃Zn@CN-G being 6.7 times that of Ni₃Zn@CN. This implies that the glycerol strengthens the interaction between C and Ni, Zn species and promotes the reduction of Ni₃ZnC_{0.7} phase. Thus, this further illustrates that the doping of glycerol and Zn can successfully promote the formation of Ni₃ZnC_{0.7} phase.

In order to further reveal the activation effect of Ni₃ZnC_{0.7} on H₂, density functional theory (DFT) calculations were carried out on Ni@CN-G and Ni₃Zn@CN-G. As seen in Fig. 5c-f, compared with -0.69 eV on Ni (111), the adsorption energies of Ni site, Zn site and C site on Ni₃ZnC_{0.7} (111) increased to -1.12 eV, -1.19 eV and -2.23 eV, respectively. It indicates that Ni₃Zn@CN-G has stronger adsorption capacity for H₂ than Ni@CN-G. Meanwhile, H₂ cannot be activated at the Zn site of Ni₃Zn@CN-G since the H-H bond length (0.75 Å) of H₂ molecule there is the same as that of free H₂ molecule. This is consistent with the catalytic experiment results of Zn@CN-G (yield 0 %). The Ni sites of Ni@CN-G and Ni₃Zn@CN-G have activated H-H bond lengths of 0.86 Å and 0.81 Å, respectively, which are much larger than 0.75 Å of free H₂ molecules. The activated H-H bond length at the C site of Ni₃Zn@CN-G is 1.76 Å, which indicates that hydrogen atom resides there. It may be that after activation at Ni site on Ni₃ZnC_{0.7}, H₂ dissociates into active hydrogen atoms, and then overflows to the C

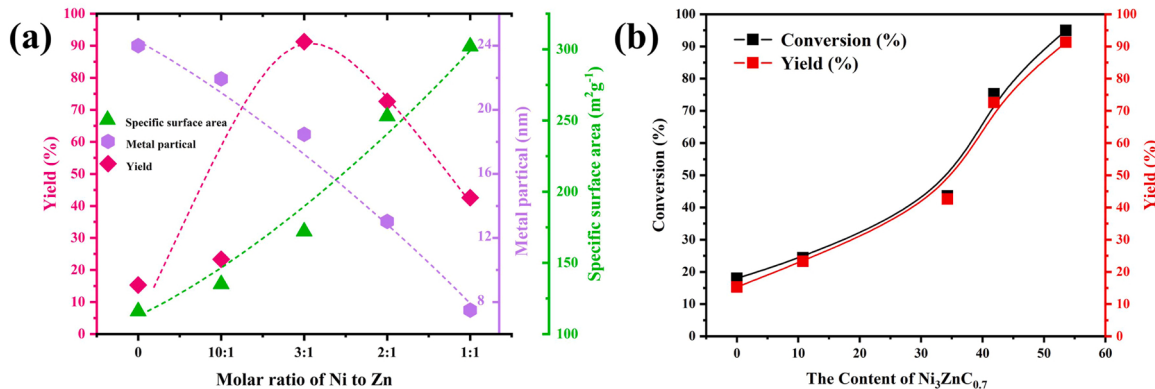


Fig. 4. (a) Plot of FOL yield, catalyst size and specific surface area versus Ni/Zn molar ratio of Ni_xZny@CN-G catalyst; (b) plot of species Ni₃ZnC_{0.7} content of versus catalytic performance.

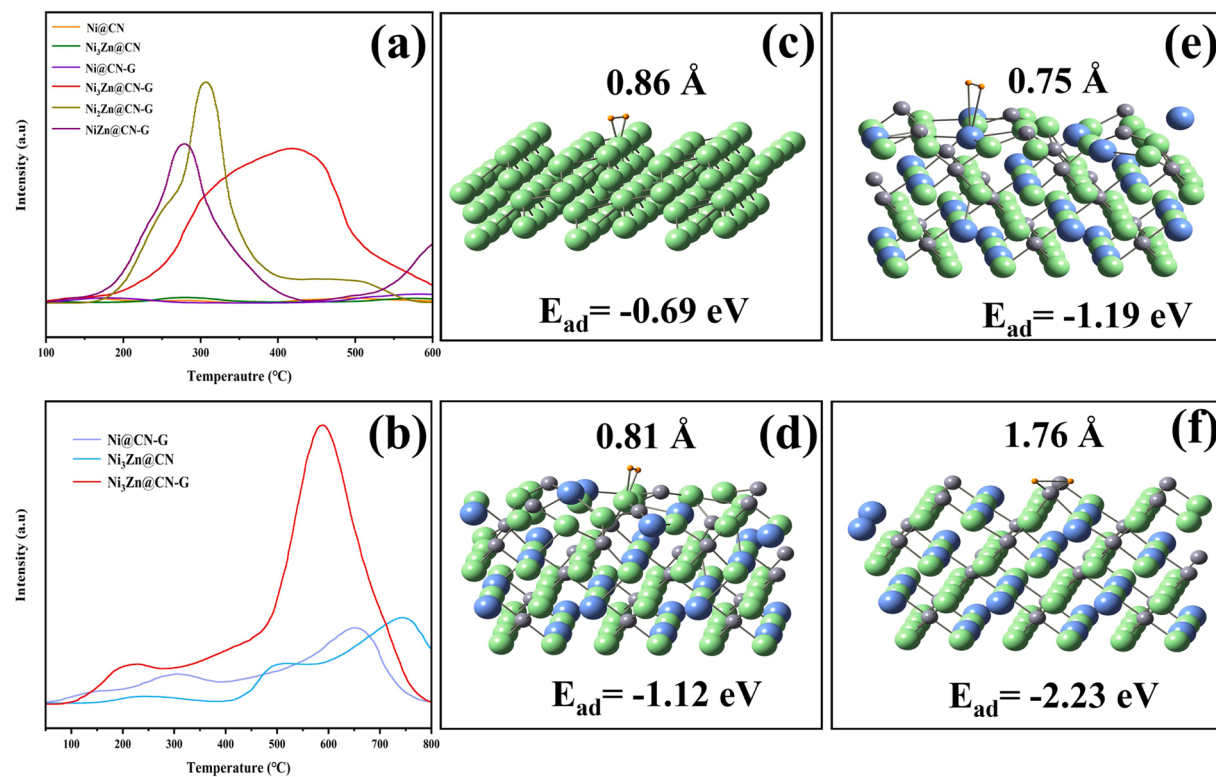


Fig. 5. (a) H₂-TPD of Ni@CN, Ni₃Zn@CN and Ni_xZn_y@CN-G; (b) H₂-TPR of Ni@CN-G, Ni₃Zn@CN, and Ni₃Zn@CN-G; (c) H₂ at Ni sites on Ni@CN-G and at Ni sites on Ni₃Zn@CN-G (d), Zn sites (e), C sites (f).

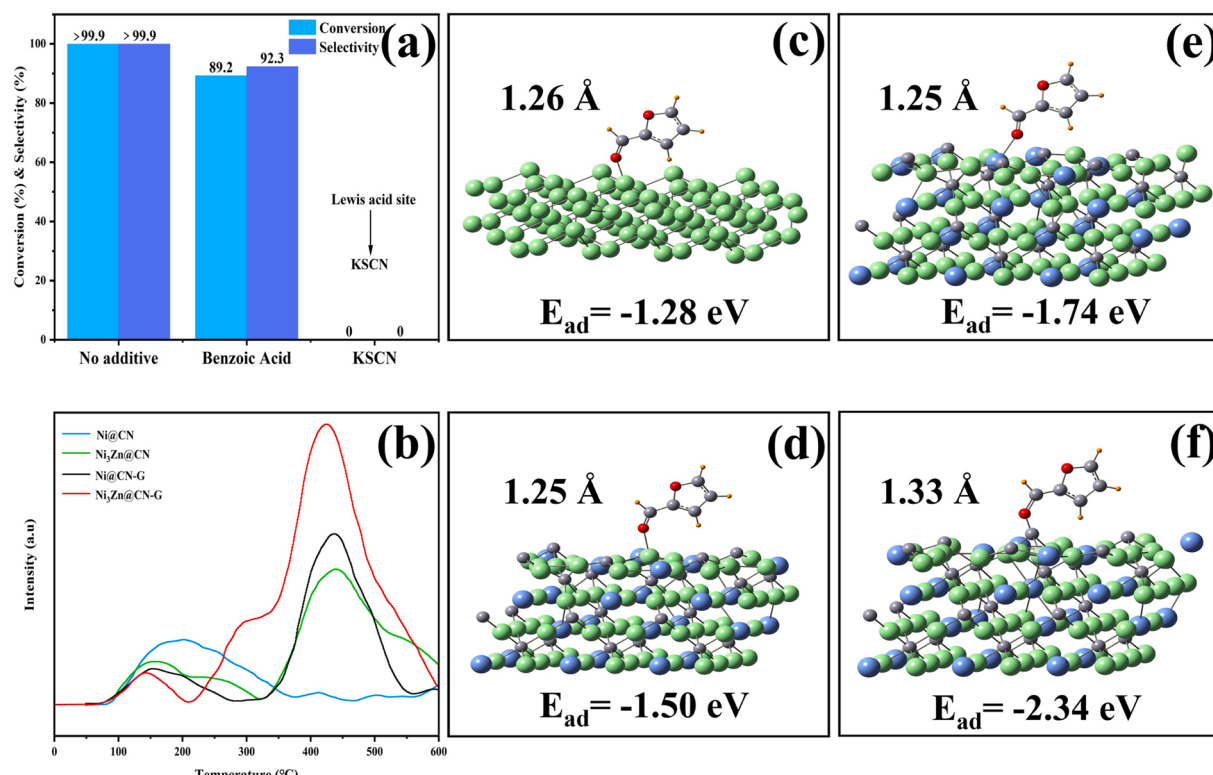


Fig. 6. (a) Toxicity experiments of Ni₃Zn@CN-G catalyst, Reaction conditions: FAL, 96 mg; catalyst, 25 mg; 2-propanol, 8 mL; H₂, 2 MPa; 120 °C; 4 h; (b) NH₃-TPD of Ni@CN, Ni₃Zn@CN, Ni@CN-G and Ni₃Zn@CN-G; (c-f) The FAL is adsorbed on Ni sites on Ni@CN-G, and Ni, Zn and C sites on Ni₃Zn@CN-G.

site [58]. From the analysis of Bader charge in Table S5, the charge after adsorption of H₂ on the Ni site increases from -0.04 |e| in Ni to the highest -0.35 |e| in Ni₃ZnC_{0.7}, indicating that the Ni in Ni₃ZnC_{0.7} interacts more strongly with H₂. According to the above results, Ni₃ZnC_{0.7} phase in Ni₃Zn@CN-G has superior H₂ activation ability compared to Ni⁰ phase of Ni@CN-G, which is consistent with the characterization findings of H₂-TPD and H₂-TPR. Therefore, the Ni₃ZnC_{0.7} phase generated by glycerol-assisted Zn content regulation enhances the activation of H₂.

3.2.3. Effect of phase composition regulation on FAL activation

Lewis acid-base sites are favorable for catalytic hydrogenation [59]. For the sake of exploring the influence of acid-base sites on the reaction, the poisoning experiment of Ni₃Zn@CN-G catalyst is carried out. The experimental results show that the Lewis base site is only a facilitator, while the Lewis acid site is essential for the hydrogenation of FAL (Fig. 6a). For further verification, the acidity of Lewis acid sites in Ni@CN, Ni₃Zn@CN, Ni@CN-G and Ni₃Zn@CN-G was characterized by NH₃-TPD (Table S7). Firstly, the effect of Zn addition on acid strength is discussed. Since NiO has a low Lewis acidity, Ni@CN only exhibits one desorption peak at 202 °C. The desorption peaks of the Ni₃Zn@CN catalyst are located at 153 °C and 439 °C. Especially the ZnO phase produces medium-strong acid at 439 °C, and its acid strength reaches 0.059 mmol g⁻¹. According to literature, stronger Lewis acid sites can promote the activation of C=O bond [60]. Similarly, Ni@CN-G and Ni₃Zn@CN-G showed desorption peaks of medium-strong acids at 437 °C and 425 °C, with acid amounts were 0.050 and 0.118 mmol g⁻¹, respectively. This indicated that the addition of Zn resulted in a 2.3 fold increase in the medium-strong acidity. Then, the impact of glycerol on acid strength was also discussed. Compared with the 0.059 mmol g⁻¹ of Ni₃Zn@CN, the addition of glycerol increased the medium-strong acid (0.118 mmol g⁻¹) of Ni₃Zn@CN-G by 2 times. It can be seen that, the stronger moderate-strong acid sites in Ni₃Zn@CN-G prepared by glycerol-assisted Zn content regulation promotes the activation of FAL.

To further explore the activation of Ni₃ZnC_{0.7} relative to FAL, the adsorption process of FAL on Ni@CN-G and Ni₃Zn@CN-G is studied by DFT. The adsorption energy of Ni and Zn sites on Ni₃Zn@CN-G increased to -1.50 eV and -1.74 eV respectively (Fig. 6d-e), from the -1.28 eV of C=O bond of FAL on Ni@CN-G (Fig. 6c), while the adsorption energy of C site reached -2.34 eV (Fig. 6f). This indicates that FAL is mainly adsorbed at the C site of Ni₃ZnC_{0.7} phase in Ni₃Zn@CN-G. According to the Bader charge analysis (Table S5), compared with the 0.60 e of C in Ni₃ZnC_{0.7}, the C site of FAL adsorption in Ni₃ZnC_{0.7} changes to -0.07 e, indicating that the positive C site in Ni₃ZnC_{0.7} has a stronger effect on FAL. Interestingly, the C=O bond length at Ni and Zn site in Ni₃Zn@CN-G is only 1.25 Å as opposed to 1.26 Å at Ni site on Ni@CN-G, while the activated C=O bond length at C site is raised to 1.33 Å. This indicates that Ni₃ZnC_{0.7} phase in Ni₃Zn@CN-G has more efficient FAL activation ability than Ni(O) phase in Ni@CN-G. The above analysis is consistent with the characterization results of NH₃-TPD. Thus, the phase composition of the catalyst was regulated by glycerol assisted Zn content, which adjusted the Lewis acid and improved the activation of FAL.

3.2.4. Effect of phase composition regulation on catalyst stability

After the reacted Ni₃Zn@CN-G catalyst is collected, it can be directly used in the next reaction of FAL hydrogenation under the same conditions without any subsequent treatment. In Fig. 7a, the activity of Ni₃Zn@CN-G decreased slightly (from >99–83 %) after the catalyst was recycled 2 times. Nevertheless, the activity remained basically unchanged after the three time. XRD results (Fig. 7b) show that there is no difference between the characteristic peaks of used and fresh catalysts. As shown in Fig. 7c, the particle size of the used Ni₃Zn@CN-G was 18.64 nm, which did not change significantly from 18.47 nm of the fresh catalyst (Fig. 3d). In XPS spectrum of used Ni₃Zn@CN-G catalyst, Zn 2p (Fig. 7d) is similar to that of fresh catalyst. While, compared with the fresh catalyst, the C 1s of the used catalyst has two more peaks of 282.5 eV and 291 eV (Fig. 7e). The binding energy of 291 eV is the conjugate bond of C [61], which is the conjugated double bond of C=C

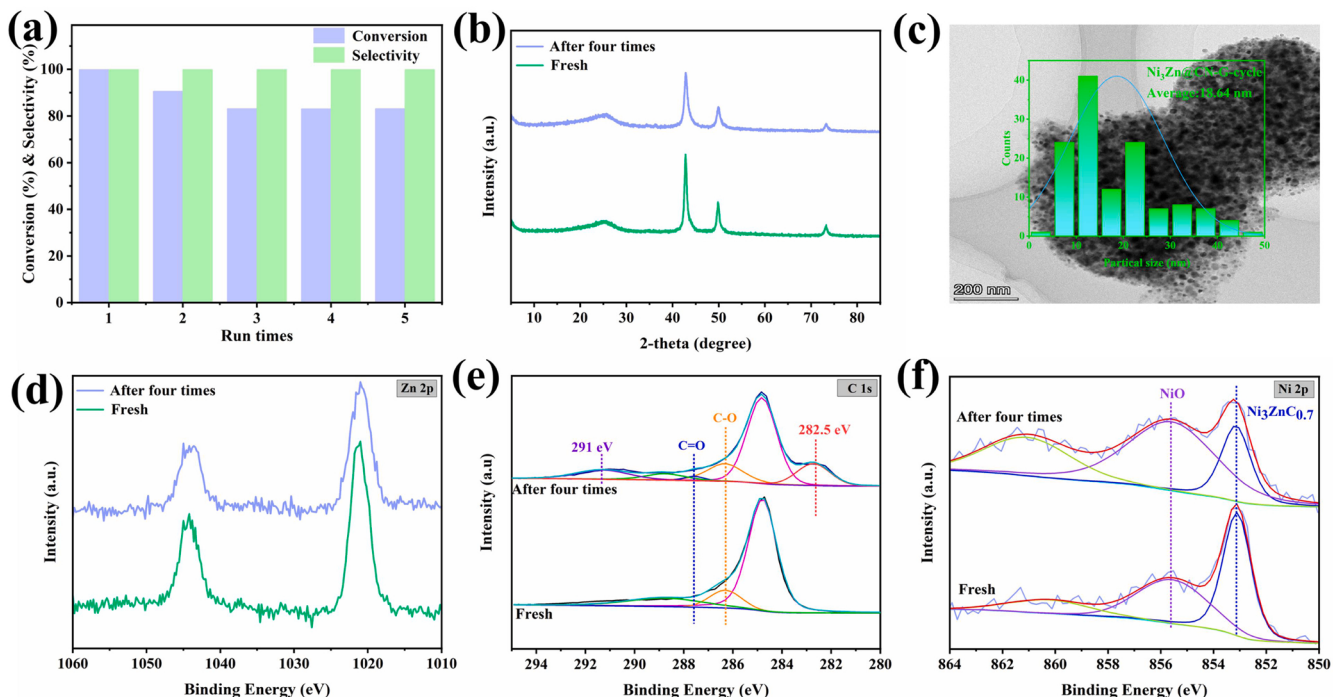


Fig. 7. (a) Cycling experiments of Ni₃Zn@CN-G catalyst; Reaction conditions: FAL, 96 mg; catalyst, 25 mg; 2-propanol, 8 mL; H₂, 2 MPa; 120 °C; 4 h; (b) XRD patterns of Ni₃Zn@CN-G catalyst after fresh and cycling four times; (c) TEM and particle size distribution of the catalyst after cycling four times; (d) XPS spectra of Zn 2p of Ni₃Zn@CN-G catalysts after fresh and four cycles; (e) XPS spectra of C 1s of Ni₃Zn@CN-G catalyst after fresh and four cycles; (f) XPS spectra of Ni 2p of Ni₃Zn@CN-G catalyst after fresh and cycling four times.

in furan ring. At the same time, the C–O strength at 286.3 eV and the C=O strength at 287.5 eV are obviously higher than that of fresh catalyst. This shows that FOL with C–O and C=C–C is adsorbed on C, resulting in a certain amount of carbon deposition. Raman spectra of the fresh and used catalysts (Fig. S4) also demonstrate slight carbon deposition [62]. In addition, the binding energy of 282.5 eV may be the carbon peak bound to Zn (ZnC) [63]. In the Ni 2p spectrum (Fig. 7f), the content of NiO is obviously higher than that of fresh catalyst. This is because the highly active Ni(0) in $\text{Ni}_3\text{ZnC}_{0.7}$ is oxidized on the surface of the catalyst to produce NiO and ZnC. Therefore, it can be inferred that the loss of active phase ($\text{Ni}_3\text{ZnC}_{0.7}$) and the coverage of oxide film (NiO) reduced the contact and activation of reaction substrate on the surface of $\text{Ni}_3\text{ZnC}_{0.7}$ active phase, which led to a slight decrease in catalytic activity. Therefore, the formation of oxide film also prevented the continuous deactivation of the active phase of $\text{Ni}_3\text{ZnC}_{0.7}$, so the activity of $\text{Ni}_3\text{ZnC}_{0.7}$ remained basically unchanged after the second catalysis.

4. Conclusion

In conclusion, a novel approach of glycerol-assisted Zn content regulation was successfully used to construct a low-cost Ni-based catalyst with a single $\text{Ni}_3\text{ZnC}_{0.7}$ phase. In comparison to Ni@CN synthesized without glycerol and Zn doping, the FOL yield increased nine times when the best $\text{Ni}_3\text{Zn@CN-G}$ was employed for selective hydrogenation of FAL to FOL. The modulation of the $\text{Ni}_3\text{ZnC}_{0.7}$ phase composition and content by glycerol-assisted Zn content is primarily responsible for the excellent catalytic performance. The catalytic characterization and DFT calculation show that $\text{Ni}_3\text{ZnC}_{0.7}$ phase can effectively promote the activation of H_2 and FAL, thus enhancing the catalytic activity and selectivity. In addition, the adjustment of glycerol and Zn content also optimized the structural characteristics of $\text{Ni}_3\text{Zn@CN-G}$ catalyst, enhanced the exposure of active sites and facilitated mass transfer. In this work, the phase composition of bimetallic carbide was effectively regulated by this strategy, which deepened the understanding of active phase in catalytic reaction. This is of great significance to the design of green catalyst and efficient conversion of biomass.

CRediT authorship contribution statement

Chunyan Yang: Paper writing. **Changfu Zhuang:** Paper Design. **Zhouxiao Zhai:** Experimental assistant. **Xu Zhao:** Experimental assistant. **Dejin Huang:** Experimental assistant. **Di Tian:** Experimental assistant. **Chungang Min:** Theoretical Calculation. **Jie Zhao:** Paper Review and Suggestions. **Ying Wang:** Paper design.

Declaration of Competing Interest

The authors declare that they have no known competing financial interests or personal relationships that could have appeared to influence the work reported in this paper.

Data Availability

Data will be made available on request.

Acknowledgements

This work was supported by the National Natural Science Foundation of China (No.31760190, 11764026, 32260368), Science and Technology Planning Project of Yunnan Province (202101BD070001-007, 202001AT070080, 202101BD070001-052, 202201AU070066), Yunnan Provincial Department of Education Fund (2022J0498, 2022Y567), Young and Middle-aged Academic and Technical Leaders Project in Yunnan Province (202205AC160052).

Appendix A. Supporting information

Supplementary data associated with this article can be found in the online version at doi:10.1016/j.apcatb.2023.122854.

References

- [1] S. Zhou, F. Daia, Z. Xiang, T. Songa, D. Liua, F. Luia, H. Qi, Zirconium-lignosulfonate polyphenolic polymer for highly efficient hydrogen transfer of biomass-derived oxygenates under mild conditions, *Appl. Catal. B: Environ.* 248 (2019) 31–43.
- [2] R. Mariscal, P. Maireles-Torres, M. Ojeda, I. Sádaba, M.L. Granadosa, Furfural: a renewable and versatile platform molecule for the synthesis of chemicals and fuels, *Energy Environ. Sci.* (2016) 1144–1189.
- [3] P. Koley, S.C. Shit, B. Joseph, S. Pollastri, Y.M. Sabri, E.L.H. Mayes, L. Nakka, J. Tardio, J. Mondal, Leveraging Cu/CuFe₂O₄-catalyzed biomass-derived furfural hydrodeoxygenation: a nanoscale metal-organic-framework template is the prime key, *ACS Appl. Mater. Interfaces* 12 (2020) 21682–21700.
- [4] S. Li, Y. Fan, C. Wu, C. Zhuang, Y. Wang, X. Li, J. Zhao, Z. Zheng, Selective hydrogenation of furfural over the Co-based catalyst: a subtle synergy with Ni and Zn dopants, *ACS Appl. Mater. Interfaces* 13 (2021) 8507–8517.
- [5] P. Zhou, Z. Zhang, L. Jiang, C. Yu, K. Lv, J. Sun, S. Wang, A versatile cobalt catalyst for the reductive amination of carbonyl compounds with nitro compounds by transfer hydrogenation, *Appl. Catal. B: Environ.* 210 (2017) 522–532.
- [6] H. Nie, H. Li, Q. Yang, D. Li, Effect of structure and stability of active phase on catalytic performance of hydrotreating catalysts, *Catal. Today* 316 (2018) 13–20.
- [7] G.S. Gautam, K.C.H. Kumara, Elastic, thermochemical and thermophysical properties of rock salt-type transition metal carbides and nitrides: a first principles study, *J. Alloy. Compd.* 587 (2014) 380–386.
- [8] J.B. Claridge, A.P.E. York, A.J. Brungs, M.L.H. Green, Study of the temperature-programmed reaction synthesis of early transition metal carbide and nitride catalyst materials from oxide precursors, *Chem. Mater.* 12 (2000) 132–142.
- [9] H.H. Hwu, J.G. Chen, Surface chemistry of transition metal carbides, *Chem. Rev.* 105 (2005) 185–212.
- [10] Y. Hara, N. Minami, H. Itagaki, Synthesis and characterization of high-surface area tungsten carbides and application to electrocatalytic hydrogen oxidation, *Appl. Cata A: Gen.* 323 (2007) 86–93.
- [11] I.G.O. Crnivec, P. Djinovic, B. Erjavec, A. Pintar, Effect of synthesis parameters on morphology and activity of bimetallic catalysts in CO₂–CH₄ reforming, *Chem. Eng. J.* 207–208 (2012) 299–307.
- [12] Q. Hu, X. Liu, B. Zhu, L. Fan, X. Chai, Q. Zhang, J. Liu, C. He, Z. Lin, Crafting MoC₂-doped bimetallic alloy nanoparticles encapsulated within n-doped graphene as robust bifunctional electrocatalysts for overall water splitting, *Nano Energy* 50 (2018) 212–219.
- [13] Y. Nakagawa, M. Tamura, K. Tomishige, Catalytic reduction of biomass-derived furanic compounds with hydrogen, *ACS Catal.* 3 (2013) 2655–2668.
- [14] D. Liang, Y. Wang, M. Chen, X. Xie, C. Li, J. Wang, L. Yuan, Dry reforming of methane over Mn-Ni/attapulgite: effect of Mn content on the active site distribution and catalytic performance, *Fuel* 321 (2022), 124032.
- [15] D.J. Siegel, J.C. Hamilton, First-principles study of the solubility, diffusion, and clustering of C in Ni, *Phys. Rev. B* 68 (2003), 094105.
- [16] S.T. Ceyer, The unique chemistry of hydrogen beneath the surface: catalytic hydrogenation of hydrocarbons, *Acc. Chem. Res.* 34 (2001) 737–744.
- [17] J.K. Norskov, T. Bligaard, J. Rossmeisl, C.H. Christensen, Towards the computational design of solid catalysts, *Nat. Chem.* 1 (2009) 37–46.
- [18] Y. Xiao, P. Sun, M. Cao, Core-shell bimetallic carbide nanparticles confined in a three-dimensional N-doped carbon conductive network for efficient lithium storage, *ACS Nano* 8 (2014) 7846–7857.
- [19] Y. Niu, X. Huang, Y. Wang, M. Xu, J. Chen, S. Xu, M.G. Willinger, W. Zhang, M. Wei, B. Zhang, Manipulating interstitial carbon atoms in the nickel octahedral site for highly efficient hydrogenation of alkyne, *Nat. Commun.* 11 (2020) 3324.
- [20] D. Teschner, E. Vass, M. Hävecker, S. Zafeiratos, P. Schnörrch, H. Sauer, A. Knop-Gericke, R. Schlögl, M. Chamam, A. Woitsch, A.S. Canning, J.J. Gamman, S. D. Jackson, J. McGregor, L.F. Gladden, Alkyne hydrogenation over Pd catalysts: a new paradigm, *J. Catal.* 242 (2006) 26–37.
- [21] X. Zhang, K. Yim, J. Kim, D. Wu, S. Ha, Elucidating the role and interplay of nickel and molybdenum carbide particles supported on Zeolite Y in methane-steam reforming, *Appl. Catal. B: Environ.* 310 (2020), 121250.
- [22] P. Hector, S. Michail, Atomistic and electronic structure of metal clusters supported on transition metal carbides: implications for catalysis, *J. Mater. Chem. A* 10 (2022) 1522–1534.
- [23] J. Gu, M. Jian, L. Huang, Z. Sun, A. Li, Y. Pan, J. Yang, W. Wen, W. Zhou, Y. Lin, H. Wang, X. Liu, L. Wang, X. Shi, X. Huang, L. Cao, S. Chen, X. Zheng, H. Pan, J. Zhu, S. Wei, W. Li, J. Lu, Synergizing metal-support interactions and spatial confinement boosts dynamics of atomic nickel for hydrogenations, *Nat. Nanotechnol.* 16 (2021) 1141–1149.
- [24] J. Yu, Y. Yang, L. Chen, Z. Li, W. Liu, E. Xu, Y. Zhang, S. Hong, X. Zhang, M. Wei, NiBi intermetallic compounds catalyst toward selective hydrogenation of unsaturated aldehydes, *Appl. Catal. B: Environ.* 277 (2020) 119273–119281.
- [25] W. Liu, Y. Yang, L. Chen, E. Xu, J. Xu, S. Hong, X. Zhang, M. Wei, Atomically-ordered active sites in NiMo intermetallic compound toward low-pressure hydrodeoxygenation of furfural, *Appl. Catal. B: Environ.* 282 (2021), 119569.

- [26] S.F. Zaman, L.A. Jolaoso, S. Podila, A.A. Al-Zahrani, Y.A. Alhamed, H. Driss, M. M. Daous, L. Petrov, Ammonia decomposition over citric acid chelated g-Mo₂N and Ni₂Mo₃N catalysts, *Int. J. Hydrogen Energy* 43 (2018) 17252–17258.
- [27] A.A. Smirnov, Z. Geng, S.A. Khromova, S.G. Zavarukhin, O.A. Bulavchenko, A. A. Saraev, V.V. Kaichev, D.Y. Ermakov, V.A. Yakovlev, Nickel molybdenum carbides: Synthesis, characterization, and catalytic activity in hydrodeoxygenation of anisole and ethyl caprate, *J. Catal.* 354 (2017) 61–77.
- [28] A. Miño, C. Lancelot, P. Blanchard, C. Lamonié, L. Rouleau, M. Roy-Auberger, S. Royer, E. Payen, Strategy to produce highly loaded alumina supported CoMo-S catalyst for straight run gas oil hydrodesulfurization, *Appl. Catal. A: Gen.* 530 (2017) 145–153.
- [29] M. Breysse, P. Afanasiev, C. Geantet, M. Vrinat, Overview of support effects in hydrotreating catalysts, *Catal. Today* 86 (2003) 5–16.
- [30] M. Li, H. Li, F. Jiang, Y. Chu, H. Nie, The relation between morphology of (Co) MoS₂ phases and selective hydrodesulfurization for CoMo catalysts, *Catal. Today* 149 (2010) 35–39.
- [31] H. Topsøe, The role of Co–Mo–S type structures in hydrotreating catalysts, *Appl. Catal. A: Gen.* 322 (2007) 3–8.
- [32] X. Fan, Z. Peng, R. Ye, H. Zhou, X. Guo, M₃C (M: Fe, Co, Ni) nanocrystals encased in graphene nanoribbons: An active and stable bifunctional electrocatalyst for oxygen reduction and hydrogen evolution reactions, *ACS Nano* 9 (2015) 7407–7418.
- [33] X. Dong, Z. Zhang, Q. Xiao, X. Zhao, Y. Chuang, Characterization of ultrafine γ-Fe (C), a-Fe(C) and Fe₃C particles synthesized by arc-discharge in methane, *J. Mater. Sci.* 33 (1998) 1915–1919.
- [34] J. Gao, Y. Wu, C. Jia, Z. Zhong, F. Gao, Y. Yang, B. Liu, Controllable synthesis of α-MoC_{1-x} and β-Mo₂C nanowires for highly selective CO₂ reduction to CO, *Catal. Commun.* 84 (2016) 147–150.
- [35] R.F.W. Bader, Atoms in molecules: a quantum theory, international series of monographs on chemistry, *Science* 252 (1990).
- [36] X. Ge, Z. Ren, Y. Cao, X. Liu, J. Zhang, G. Qian, X. Gong, L. Chen, X. Zhou, W. Yuan, X. Duan, Enhanced acetylene semi-hydrogenation on a subsurface carbon tailored Ni–Ga intermetallic catalyst, *J. Mater. Chem. A* 10 (2022) 19722–19731.
- [37] X. Kong, Y. Zhu, H. Zheng, Y. Zhu, Z. Fang, Inclusion of Zn into metallic Ni enables selective and effective synthesis of 2,5-dimethylfuran from bioderived 5-hydroxymethylfurfural, *ACS Sustain. Chem. Eng.* 5 (2017) 11280–11289.
- [38] Y. Li, X. Cai, S. Chen, H. Zhang, H. Zhang, J. Hong, B. Chen, D. Kuo, W. Wang, Highly dispersed metal carbide on ZIF-derived pyridinic-N-doped carbon for CO₂ enrichment and selective hydrogenation, *ChemSusChem* 11 (2018) 1040–1047.
- [39] Y. Wang, B. Liu, X. Lan, T. Wang, Subsurface carbon as a selectivity promotor to enhance catalytic performance in acetylene semihydrogenation, *ACS Catal.* 11 (2021) 10257–10266.
- [40] Z. Yang, F. Wang, Differentiation of alkane isomers through binding energy spectra and total momentum cross sections, *New J. Chem.* 38 (2014) 1031.
- [41] G. Nan, E. Papirer, P. Fioux, F. Mgguet, A. Trbssaud, Fluorination of carbon blacks: an X-ray photoelectron spectroscopy study: I. A literature review of XPS studies of fluorinated carbons. XPS investigation of some reference compounds, *Carbon* 35 (1997) 175–194.
- [42] P.P. Paalanen, S.H. Vreeswijk, B.M. Weckhuysen, Combined *in situ* X-ray powder diffractometry/raman spectroscopy of iron carbide and carbon species evolution in Fe(–Na–S)/α-Al₂O₃ catalysts during Fischer–Tropsch synthesis, *ACS Catal.* 10 (2020) 9837–9855.
- [43] O.A. Maslova, M.R. Ammar, G. Guimbret'ere, J.-N. Rouzaud, P. Simon, Determination of crystallite size in polished graphitized carbon by Raman spectroscopy, *Phys. Rev. B* 86 (2012), 134205.
- [44] C. Celebi, C. Yanik, A.G. Demirkol, I.I. Kaya, The effect of a SiC cap on the growth of epitaxial graphene on SiC in ultra high vacuum, *Carbon* 50 (2012) 3026–3031.
- [45] Z.H. Ni, W. Chen, X.F. Fan, J.L. Kuo, T. Yu, A.T.S. Wee, Z.X. Shen, Raman spectroscopy of epitaxial graphene on a SiC substrate, *Phys. Rev. B* 77 (2008), 115216.
- [46] L.H. Zhang, Y. Shi, Y. Wang, N.R. Shiju, Nanocarbon catalysts: recent understanding regarding the active sites, *Adv. Sci.* 7 (2020), 1902126.
- [47] Q. Liu, L. Wang, M. Chen, Y. Cao, H. He, K. Fan, Dry citrate-precursor synthesized nanocrystalline cobalt oxide as highly active catalyst for total oxidation of propane, *J. Catal.* 263 (2009) 104–113.
- [48] H. Huang, R. Zong, H. Li, Synergy effects between oxygen groups and defects in hydrodeoxygenation of biomass over a carbon nanosphere supported Pd catalyst, *ACS Sus. Chem. Eng.* 8 (2020) 15998–16009.
- [49] B. Rivas-Murias, V. Salgueirino, Thermodynamic CoO–Co₃O₄ crossover using Raman spectroscopy in magnetic octahedron shaped nanocrystals, *J. Raman Spectrosc.* 48 (2017) 837–841.
- [50] Y. Liu, B. Chen, R. Liu, W. Liu, X. Gao, Y. Tan, Z. Zhang, W. Tu, CO₂ hydrogenation to olefins on supported iron catalysts: Effects of support properties on carbon-containing species and product distribution, *Fuel* 324 (2022), 124649.
- [51] X. Cui, Y. Shen, Q. Yang, S. Kawi, Z. He, X. Yang, C.H. Wang, Simultaneous syngas and biochar production during heavy metal separation from Cd/Zn hyperaccumulator (*Sedum alfredii*) by gasification, *Chem. Eng. J.* 347 (2018) 543–551.
- [52] Y. Fan, S. Li, Y. Wang, C. Zhuang, X. Liu, G. Zhu, X. Zou, Tuning the synthesis of polymetallic-doped ZIF derived materials for efficient hydrogenation of furfural to furfuryl alcohol, *Nanoscale* 12 (2020) 18296–18304.
- [53] J. Chu, Y. Fan, L. Sun, C. Zhuang, Y. Li, X. Zou, C. Min, X. Liu, Y. Wang, G. Zhu, Exploring the Zn-regulated function in Co–Zn catalysts for efficient hydrogenation of ethyl levulinate to γ-valerolactone, *Catal. Sci. Technol.* 12 (2022) 4325.
- [54] Z. Zhai, J. Chu, L. Sun, X. Zhao, D. Huang, X. Yang, C. Zhuang, C. Min, Y. Wang, Ultrahigh metal content carbon-based catalyst for efficient hydrogenation of furfural: the regulatory effect of glycerol, *ACS Appl. Mater. Interfaces* 14 (2022) 44439–44449.
- [55] H. Tian, X. Liu, L. Dong, X. Ren, H. Liu, C.A.H. Price, Y. Li, G. Wang, Q. Yang, J. Liu, Enhanced hydrogenation performance over hollow structured Co-CoO_x@N-C capsules, *Adv. Sci.* 6 (2019), 1900807.
- [56] B. You, N. Jiang, M. Sheng, W.S. Drisdell, J. Yano, Y. Sun, Bimetal-organic framework self-adjusted synthesis of supportfree nonprecious electrocatalysts for efficient oxygen reduction, *ACS Catal.* 5 (2015) 7068–7076.
- [57] M.M. Bettahar, The hydrogen spillover effect. A misunderstanding story, *Catal. Rev.* 64 (2022) 87–125.
- [58] S.A. Rasakia, Z. Chen, T. Thomas, M. Yang, Anti-perovskite metal carbides: a new family of promising electrocatalysts for oxygen reduction in alkaline solution, *Mater. Res. Bull.* 133 (2020), 111014.
- [59] M. Puche, L. Liu, P. Concepcion, I. Sorribes, A. Corma, Tuning the Catalytic Performance of Cobalt Nanoparticles by Tungsten Doping for Efficient and Selective Hydrogenation of Quinolines under Mild Conditions, *ACS Catal.* 11 (2021) 8197–8210.
- [60] L. Wang, Y. Yang, P. Yin, Z. Ren, W. Liu, Z. Tian, Y. Zhang, E. Xu, J. Yin, M. Wei, MoO_x-decorated Co-based catalysts toward the hydrodeoxygenation reaction of biomass-derived platform molecules, *ACS Appl. Mater. Interfaces* 13 (2021) 31799–31807.
- [61] A.P. Dementjev, K.I. Maslakov, Possibilities of C 1s XPS and N(E) C KVV Auger spectroscopy for identification of inherent peculiarities of diamond growth, *Appl. Surf. Sci.* 253 (2006) 1095–1100.
- [62] A.L.A. Marinho, R.C. Rabelo-Neto, F. Epron, N. Bion, F.S. Toniolo, F.B. Noronha, Embedded Ni nanoparticles in CeZrO₂ as stable catalyst for dry reforming of methane, *Appl. Catal. B: Environ.* 268 (2020).
- [63] H. Pan, J. Yi, L. Shen, R. Wu, J. Yang, J. Lin, Y. Feng, J. Ding, L. Van, J. Yin, Room-temperature ferromagnetism in carbon-doped ZnO, *Phys. Rev. Lett.* 99 (2007), 127201.